

A Lung Graph–Model for Pulmonary Hypertension and Pulmonary Embolism Detection on DECT Images

Yashin Dicente Cid^{1,2}, Henning Müller^{1,2,3}, Alexandra Platon⁴, Jean–Paul Janssens⁴, Frédéric Lador⁴, Pierre–Alexandre Poletti⁴, and Adrien Depeursinge^{1,5}

¹ University of Applied Sciences Western Switzerland (HES–SO), Sierre, Switzerland;

² University of Geneva, Switzerland;

³ Martinos Center for Biomedical Imaging, Charlestown, MA, USA;

⁴ University Hospitals of Geneva (HUG), Switzerland;

⁵ École Polytechnique Fédérale de Lausanne (EPFL), Switzerland;

Email: yashin.dicente@hevs.ch

Abstract. This article presents a novel graph–model approach encoding the relations between the perfusion in several regions of the lung extracted from a geometry–based atlas. Unlike previous approaches that individually analyze regions of the lungs, our method evaluates the entire pulmonary circulatory network for the classification of patients with pulmonary embolism and pulmonary hypertension. An undirected weighted graph with fixed structure is used to encode the network of intensity distributions in Dual Energy Computed Tomography (DECT) images. Results show that the graph–model presented is capable of characterizing a DECT dataset of 30 patients affected with disease and 26 healthy patients, achieving a discrimination accuracy from 0.77 to 0.87 and an AUC between 0.73 and 0.86. This fully automatic graph–model of the lungs constitutes a novel and effective approach for exploring the various patterns of pulmonary perfusion of healthy and diseased patients.

Keywords: Lung graph–model, lung atlas, computer–aided diagnosis, pulmonary perfusion.

1 Introduction

In an emergency department, a patient with a pulmonary vascular pathology requires a quick and reliable diagnosis to proceed with the corresponding treatment and symptoms for many diseases are often unspecific. Currently, health professionals face a difficult task to distinguish between the different types of pathologies, such as pulmonary embolism (PE) and pulmonary hypertension (PH) [9]. Both pathologies present similar symptoms and visual radiological defects but require completely different treatments. The current gold standard for diagnosing pulmonary hypertension requires an invasive catheterism procedure [11, 12, 22]. In addition, most patients in the emergency department undergo a routine Computed Tomography (CT) thorax scan with contrast agent.

The visual interpretation of the latter is challenging as it involves a holistic analysis of the pulmonary perfusion. Schickert et al. [18] confirmed that CT image analysis allows detection of chronic thromboembolism. PE and PH have similar visual signs, showing in some cases mosaic patterns due to the hypo- and hyper-perfused regions as a consequence of clots in the vascular tree. Dual Energy CT (DECT) scans have shown to allow quantifying perfusion defects of the lung parenchyma [2, 13, 14, 19, 20] using iodine components derived from CT attenuation at two energy levels of 80 and 140 keV. Several studies have presented region-based approaches to analyze the parenchyma [6, 7]. However, to the best of our knowledge, no work has tried to detect pulmonary vascular diseases based on the comparison of the regions, allowing a holistic analysis of the pulmonary system. This article is based on the hypothesis that when a region is hypo-perfused due to a clot, another region or regions may absorb the excess of blood-flow, creating hyper-perfused regions [1]. Our method consists of dividing the lungs into 36 geometrical regions and comparing the perfusion of each pair of regions. In the case of healthy patients, the hypothesis is that the distribution of the perfusion should be similar across patients, presenting a radial pattern with maximum perfusion in regions close to the heart and minimum perfusion in the peripheral regions.

The selected technique to characterize these relations is an undirected weighted graph with a fixed structure. Graph-models have been widely used in medical imaging [15, 17, 21, 24], particularly in functional brain analysis. Some graph-methods on brain image analysis consist of dividing the brain into fixed functional regions. Then, the relations between the activation of these regions are compared [16]. In this work, we use a similar approach for the lungs where geometric regions are used instead of the functional regions, and instead of analyzing the co-activation of different zones, we compare their perfusion. To the best of our knowledge, this work constitutes a first attempt to provide holistic characterizations of the lung perfusion based on anatomical graph models from CT image analysis.

2 Methods

2.1 Dataset

Experiments were carried out on contrast-enhanced chest DECT images of 56 patients, 17 with diagnosed PE, 13 with diagnosed PH and 26 control cases (CC). The institutional ethics committee agreed on the study. PH patients were taken from an ongoing PH study, PE and control cases were taken from clinical routine cases in the emergency department and control cases were chosen to be similar in terms of age distribution to the other categories. DECT images were obtained with a Discovery CT750 HD from General Electric Medical Systems. 11 energy levels were chosen from each DECT image, from 40 keV to 140 keV in steps of 10 keV, yielding 4D data with intensities measured in Hounsfield Units (HU). The resolution of the DECT slices varied from 0.6289 to 0.9766 mm, while the inter-slice distance was 1.00 mm.

2.2 Graph-Model

The lung volumes were automatically segmented from the DECT images using the method explained in [8]. This method achieved the best results in the lung-segmentation task for CT images in the VISCERAL Anatomy Challenge 2015 [10]. Only the 70 keV level of the DECT images was used to compute the lung segmentation. Once the lungs were segmented, the atlas presented in [6] was computed on the segmented lung mask (see Figure 1). The same atlas mask was used for all the energy levels of the DECT image. The atlas contains 36 geometric regions produced by intersecting four axis segmentations: coronal (right/left), sagittal (anterior/posterior), vertical (apical/central/basal), and axial (peripheral/middle/central). These locations are based on the 3D model of the lung presented by Zrimec et al. [25]. This atlas provides adequate partitioning, grouping areas with vessels of similar size, and thus, **similar texture**. Moreover, it considers the peripheral regions separately, which are mainly affected by PH. An anatomic separation based on lobes would be another possibility but it is sometimes difficult and error prone in patients with strong pathologies, such as the patients we are analyzing. It is also much slower to compute.

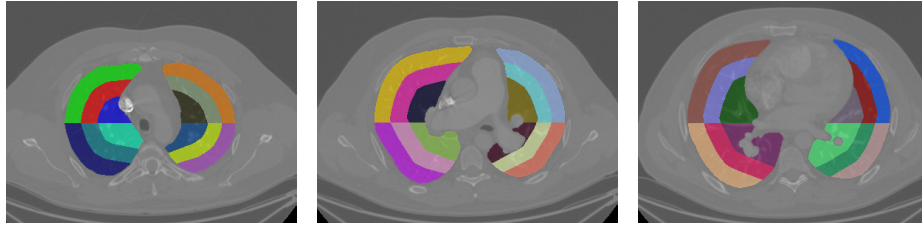


Fig. 1: Three axial views of the same DECT image at different heights showing the 36-geometrical-region atlas used to divide the lungs. The example corresponds to the 70 keV energy level of a PH patient DECT scan. Please refer to Figure 2a for a 3D visualization of the atlas.

Every region was characterized using the first four statistical moments of the HU distribution, i.e. mean, variance, skewness and kurtosis. The mean and the variance have a direct interpretation considering our hypothesis. Hypo- and hyper-perfused areas have high and low mean HU, respectively. A region with a clot has a vessel partially well perfused, and hence, a high variance in the region.

These measures were computed for each of the 11 energy levels of the DECT images. Each energy level corresponds to a reconstructed image generated from two mother images acquired at 80 and 140 keV. However, since the attenuation curve of each component is not linear, the information contained in the 11 levels cannot be reduced to two single values. The feature vector describing a single region was defined as the 44 dimensional vector (11 energy levels \times 4 statistics) containing the concatenation of the four statistical moments of every energy level. Let $HU(r)$ be the HU in a region r , $m(r) = Mean(HU(r))$,

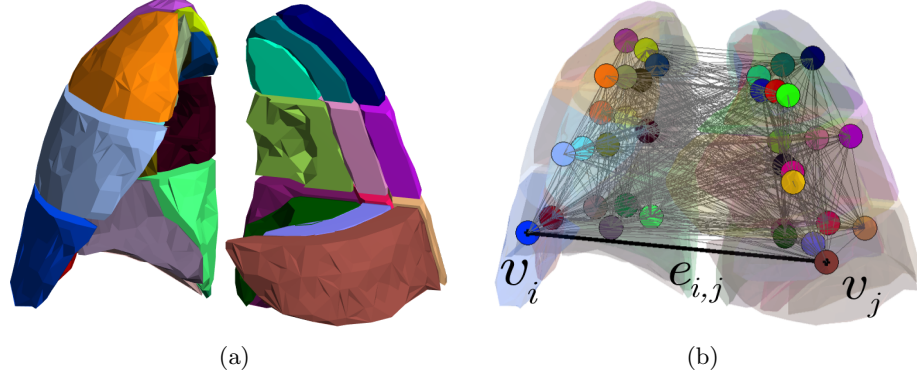


Fig. 2: Prototype visualization of the graph-model based on the 36-region atlas. 2a) 3D visualization of the 36-region atlas corresponding to the same PH patient as in Figure 1. Six regions are not visible in the visualization to show the interior atlas divisions. 2b) Undirected complete graph built from the 36-region atlas. The color of the vertices correspond to the color of the respective region in Figures 1 and 2a. v_i and v_j are the vertices corresponding to regions r_i and r_j respectively. $e_{i,j}$ is the edge connecting the vertices v_i and v_j . As it is an undirected weighted graph, $e_{i,j} = e_{j,i}$. The edge weights are defined in the adjacency matrix \mathbf{A} as $A_{i,j} = d(f(r_i), f(r_j))$, where $f(r)$ is the statistics-based feature vector of the region r (see Equation 2). All the edges between vertices are shown in light gray.

$v(r) = \text{Var}(HU(r))$, $s(r) = \text{Skew}(HU(r))$, and $k(r) = \text{Kurt}(HU(r))$. The feature vector of a region ($f(r)$) is defined as

$$f(r) = (m_{40}(r), v_{40}(r), s_{40}(r), k_{40}(r), \dots, m_{140}(r), v_{140}(r), s_{140}(r), k_{140}(r)), \quad (1)$$

where the sub-index corresponds to the energy level in keV.

The 36 regions of the atlas were considered as a fixed set of vertices V allowing comparisons between patients. The Euclidean distances between the respective feature vectors of region pairs (r_i, r_j) were considered as weights on a set of edges E . This allows the construction of an undirected complete weighted graph $\mathcal{G} = (V, E)$, with adjacency matrix $\mathbf{A} \in \mathbb{R}^{36 \times 36}$ defined as

$$A_{i,j} = d(f(r_i), f(r_j)) = \|f(r_i) - f(r_j)\|. \quad (2)$$

\mathbf{A} is symmetric because Euclidean distances were used ($A_{i,j} = A_{j,i}$). Figure 2 contains a 3D visualization of the construction of the graph from the 36-region atlas. A visualization of five adjacency matrices for each class in the dataset (CC, PE, and PH) is shown in Figure 3.

The use of a complete graph provides a full holistic characterization of the lungs. This is particularly useful when only one lung is healthy and the other

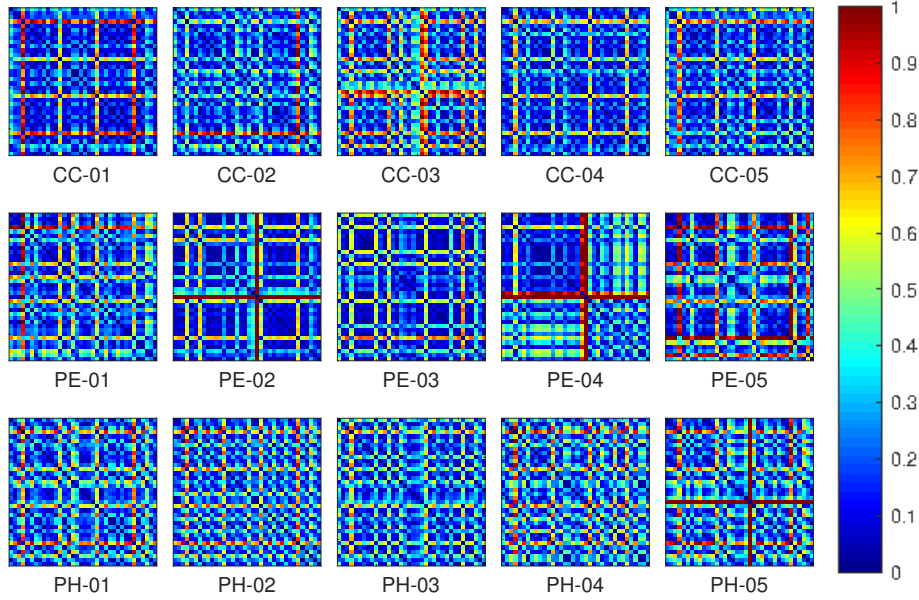


Fig. 3: Patient-wise graph adjacency matrices \mathbf{A} containing the Euclidean distances between feature vectors of each region pair. Five matrices per class (CC, PE, and PH) are shown. The distances were normalized between 0 and 1 according to the maximum and minimum distance found in the 12 example matrices. In some cases, it is possible to see patterns characteristic of each class (e.g., PE-02 and PE-04 present a characteristic red cross), but visually it is difficult to find a common discriminative pattern across entire classes.

one is homogeneously affected. The edges between regions on different lungs will highlight the affection in this case.

2.3 Graph Classification

As we are working with graphs with a fixed number of vertices, we do not require any graph-specific measure. The comparison between two graphs can be reduced to the comparison of the edge-weights encoded in the adjacency matrix. Since the vertex ordering is the same for all patients and the adjacency matrices are symmetric, they are fully characterized by their upper triangles. Hence, we use the vectorized upper triangle of the adjacency matrix as a descriptor vector of the patient. The diagonal is not used as it contains zeros only (see Equation 2). The resulting vector is then $35 + \dots + 1 = 630$ dimensional. The vectors are subsequently used in a 2-class support vector machine (SVM) [4] classifier with a linear kernel. The LIBSVM library [3] is used in all our tests. The feature space spans \mathbb{R}^{630} , where every dimension corresponds to one edge in the graph.

Four experiments are described in this article: a) CC vs. PE, b) CC vs. PH, c) PE vs. PH, and d) CC vs. non-CC, where the non-CC were composed of PH and PE.

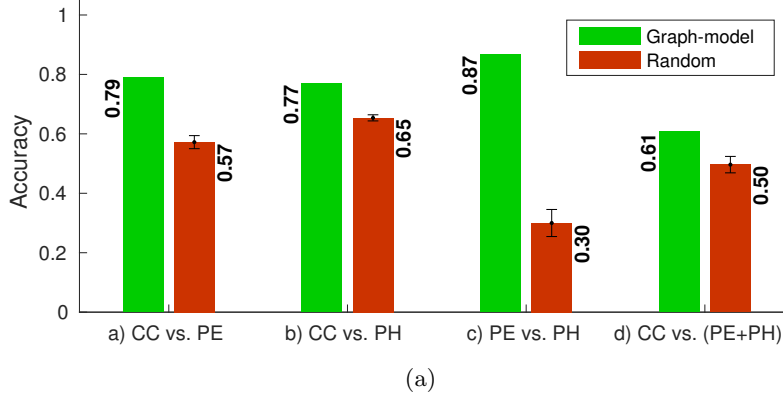
2.4 Experimental Setup

Linear SVMs only have the cost parameter C requiring optimization. The optimization phase is not straightforward when working with small datasets due to the high influence of the random division of the patient set into train, validation, and test sets. Experiment a) contained 43 patients, experiment b) 39, experiment c) 30, and experiment d) 56. For each experiment, a global leave-one-patient-out (LOPO) cross-validation (CV) was used. For each fold of the LOPO, an inner 10-fold CV was used to find the optimal value of C with a grid-search on $C = [2^{-10}, 2^{10}]$ and a logarithmic step of 0.5. At the end of the LOPO loop, all patients were classified. The accuracy and the area under the receiver operating characteristic (ROC) curve (AUC) based on the decision function of the SVM are used as performance measures.

3 Results

Figures 4 and 5 show the results for the four experiments performed. For every experiment, the accuracy and the AUC are shown in each image respectively. Because the dimension of the feature space (630) with respect to the size of the dataset is relatively high, the performance when using a randomly-generated 630-dimensional feature vector was evaluated to test the bias linked to the large feature space. The method called “Random” in Figures 4 and 5 corresponds to 10 Monte-Carlo (MC) repetitions of every experiment using random feature vectors and then the same learning procedure. In this case, the measures shown correspond to the accuracy and AUC values averaged over the 10 executions, and are referred to as random accuracy and random AUC, respectively. The ROC curves corresponding to each experiment are shown in Figure 5a. Moreover, Figure 4b shows the one tailed p -values when comparing our method against the random experiment.

The best accuracy was achieved in experiment b), PE vs. PH, with an accuracy of 0.87, while the random accuracy of this experiment was the lowest. Moreover, the p -value in this case is $2.9e-10$, highlighting statistically significant results. In experiment a), CC vs. PE, the difference between the random and the graph-model accuracies was smaller, from 0.57 to 0.79, but it is still significant with a standard confidence interval of 5 % (0.0025). Finally, experiments b) and d) had low accuracy when compared to the random accuracy, achieving 0.77 and 0.61 respectively. In these cases, the p -values are of 0.0632 and 0.0651 and are thus not significant with a confidence interval of 5 %. The small data set makes it harder to reach significance. In addition, the AUC provided information about the reliability of the classification. In this case, experiments a), b) and c) had a high AUC with respect to the random AUC. When comparing PE vs. PH and vs.



	a) CC vs. PE	b) CC vs. PH	c) PE vs. PH	d) CC vs. (PE+PH)
<i>p</i> -value	0.0025	0.0651	2.9e-10	0.0632

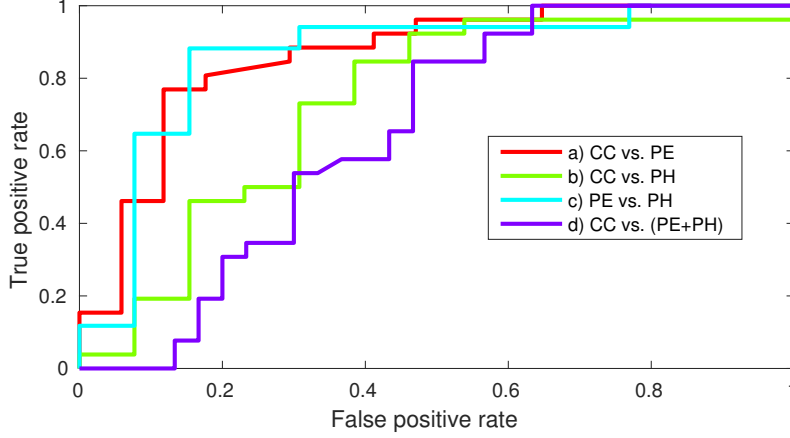
(b)

Fig. 4: Results obtained in the four experiments: a) CC vs. PE, b) CC vs. PH, c) PE vs. PH, and d) CC vs. non-CC (PE+PH). 4a) Accuracy for all four experiments. The results of the graph-model are depicted in green while the performance of a random approach is in red. The random accuracy correspond to the accuracy averaged over of 10 executions with randomly generated feature vectors. In this case, the standard error is also shown. 4b) One tailed p -values when comparing our method against the random approach.

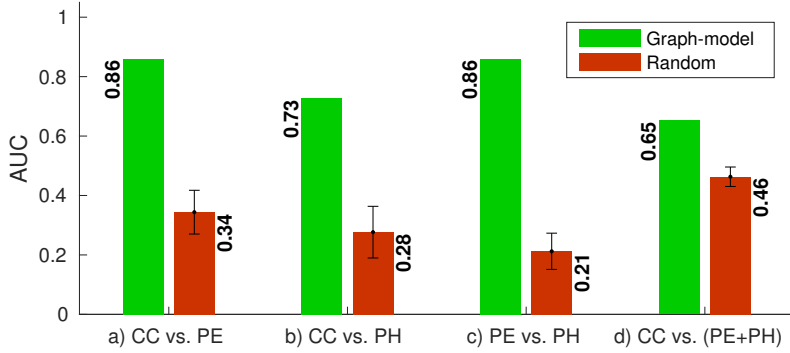
CC, the graph-model achieved an AUC of 0.86 in both cases, while experiment b), PH vs. CC, achieved 0.73. As expected from the results, experiment d) was the least reliable achieving an AUC of 0.65.

4 Discussion

Basic statistical features were used to encode HU distributions as regional descriptors of the perfusion. Features were extracted from 4D DECT images, containing the attenuation of 11 energy levels for each voxel and providing rich information of HU intensity distributions. Results show that the analysis of the relation between these statistical descriptors contained sufficient information to build a graph-model able to differentiate between PE, PH, and healthy patients. The 36-geometrical-region atlas shows to be a suitable division of the lungs to build the graph. The advantage of using a geometrical atlas instead of an anatomical atlas, e.g., based on lobes, is the possibility to build it automatically, quickly and reliably. Although some anatomical atlases based on lung lobes can be computed automatically [23], the methods often do not work for all kind of patients (i.e., with diseases or older patients).



(a)



(b)

Fig. 5: Results obtained in the four experiments: a) CC vs. PE, b) CC vs. PH, c) PE vs. PH, and d) CC vs. non-CC (PE+PH). 5a) ROC curves. 5b) AUC for all four experiments. The results of the graph-model are depicted in green while the performance of a random approach is in red. The random AUC correspond to AUC values averaged over of 10 MC executions with randomly-generated feature vectors. In this case, the standard error is also shown.

The presented technique describes the relations between regions, not considering the absolute perfusion of the region. This property can be an advantage when comparing CT scans acquired with different protocols because it provides a holistic analysis of the lungs. Moreover, any other perfusion descriptor, such as texture, can easily be added as a property of a region (graph vertex).

Every patient was described with only one single vector, the vectorized upper triangle of the adjacency matrix \mathbf{A} (Section 2.3). Due to this procedure, the small

size of the dataset was an inconvenience when splitting the dataset during the evaluation step (Section 2.4). However, DECT is not the most common imaging diagnostic choice for PE and PH patients and finding specific patients was not an easy task. To the best of our knowledge, there is no previous automatic classification-work using PH patients and no comparison with previous work was easily possible. The results of this article are an initial step in the automatic classification of PH patients based on image data alone. In the case of PE, other classification-approaches have been presented but the methods usually provided classification of local regions and the methods were designed based only on PE, while the graph-model presented may be applied to any pulmonary vascular disease.

PH experts are currently unable to identify PH patients only using DECT. A catheterization to diagnose/discard PH is required but invasive and thus not always done, missing to find the correct diagnosis for several patients. Therefore, comparing the performance of our approach against randomly generated feature vectors is a viable baseline of human diagnosis by visual inspection. We generated random vectors with the same dimensionality and with the same range of values as the features used and classify them using the same SVM. This is a reasonable comparison to learn on random feature vectors as this takes into account potential bias linked to the large feature space.

5 Conclusions and Future Work

In this article we present a novel, fully automatic graph-model of the lungs capable of discriminating between PE, PH, and healthy patients with an accuracy above 0.77, and an AUC above 0.73. The results confirmed the initial hypothesis that a graph-model encoding the perfusion distribution across lung regions characterizes PE and PH patients effectively. Graph-modeling is a complete framework widely studied that opens new possibilities for lung modeling. First of all, graphs enable inclusion of other regional features such as texture to encode the local morphological properties of lung tissue. It is also possible to generate 3D colored graph-models to help physicians in their diagnosis (Figure 2b). These 3D models can reveal information about the abnormal relations and localize the regions affected.

The method presented is simple and with very small computational cost and it would therefore scale very well. The small number of patients is a limitation of this work and we intent to further validate our model on a larger cohort. As a next step, we plan to analyze which relations in the graph best characterize each patient-class, providing more synthetic graphs for each pathology. We also plan to use the graph models to differentiate interstitial lung disease, where holistic image analysis of thoracic CT showed promising results in [5].

Acknowledgments This work was partly supported by the Swiss National Science Foundation with the PH4D (320030-146804) and MAGE projects (PZ00P2.154891).

References

1. Burrowes, K., Tawhai, M., Clark, A.: Blood flow redistribution and ventilation-perfusion mismatch during embolic pulmonary arterial occlusion. *Pulmonary Circulation* 1(3), 365 (2011)
2. Chae, E.J., Seo, J.B., Jang, Y.M., Krauß, B., Lee, C.W., Lee, H.J., Song, K.S.: Dual-energy CT for assessment of the severity of acute pulmonary embolism: Pulmonary perfusion defect score compared with CT angiographic obstruction score and right ventricular/left ventricular diameter ratio. *American Journal of Roentgenology* 194(3), 604–610 (2010)
3. Chang, C.C., Lin, C.J.: LIBSVM: A library for support vector machines. *ACM Transactions on Intelligent Systems and Technology* 2(3), 1–27 (May 2011)
4. Cortes, C., Vapnik, V.: Support-vector networks. *Machine Learning* 20(3), 273–297 (September 1995)
5. Depeursinge, A., Chin, A.C., Leung, A.N., Terrone, D., Bristow, M., Rosen, G., Rubin, D.L.: Automated classification of usual interstitial pneumonia using regional volumetric texture analysis in high-resolution CT. *Investigative Radiology* 50(4), 261–267 (April 2015)
6. Depeursinge, A., Zrimec, T., Busayarat, S., Müller, H.: 3D lung image retrieval using localized features. In: *Medical Imaging 2011: Computer-Aided Diagnosis*. vol. 7963, p. 79632E. SPIE (February 2011)
7. Dicente Cid, Y., Depeursinge, A., Foncubierta-Rodríguez, Platon, A., Poletti, P.A., Müller, H.: Pulmonary embolism detection using localized vessel-based features in dual energy CT. In: *SPIE Medical Imaging. International Society for Optics and Photonics* (2015)
8. Dicente Cid, Y., Jiménez-del Toro, O.A., Depeursinge, A., Müller, H.: Efficient and fully automatic segmentation of the lungs in CT volumes. In: Goksel, O., et al. (eds.) *Proceedings of the VISCERAL Challenge at ISBI*. No. 1390 in *CEUR Workshop Proceedings* (Apr 2015)
9. Farber, H.: Pulmonary circulation: Diseases and their treatment. 3rd edition. *European Respiratory Review* 21(123), 78–78 (2012)
10. Goksel, O., Foncubierta-Rodríguez, A., Jiménez-del Toro, O.A., Müller, H., Langs, G., Weber, M.A., Menze, B., Eggel, I., Gruenberg, K., Winterstein, M., Holzer, M., Krenn, M., Kontokotsios, G., Metallidis, S., Schaer, R., Taha, A.A., Jakab, A., Salas Fernandez, T., Hanbury, A.: Overview of the VISCERAL challenge at ISBI 2015. In: Goksel, O., et al. (eds.) *Proceedings of the VISCERAL Challenge at ISBI*. pp. 6–11. No. 1390 in *CEUR Workshop Proceedings* (Apr 2015)
11. Kim, N.H., Delcroix, M., Jenkins, D.P., Channick, R., Darteville, P., Jansa, P., Lang, I., Madani, M.M., Ogino, H., Pengo, V., Mayer, E.: Chronic thromboembolic pulmonary hypertension. *Journal of the American College of Cardiology* 62(25 SUPPL.) (2013)
12. Lador, F., Beghetti, M., Rochat, T.: Détection et traitement précoce de l'hypertension artérielle pulmonaire. *Revue Médicale Suisse* 5, 2317–2321 (2009)
13. Lee, C., Seo, J., Song, J.W., Kim, M.Y., Lee, H., Park, Y., Chae, E., Jang, Y., Kim, N., Krauß, B.: Evaluation of computer-aided detection and dual energy software in detection of peripheral pulmonary embolism on dual-energy pulmonary CT angiography. *European Radiology* 21(1), 54–62 (2011)
14. Nakazawa, T., Watanabe, Y., Hori, Y., Kiso, K., Higashi, M., Itoh, T., Naito, H.: Lung perfused blood volume images with dual-energy computed tomography for chronic thromboembolic pulmonary hypertension: Correlation to scintigraphy

with single-photon emission computed tomography. *Journal of Computer Assisted Tomography* 35(5), 590–595 (2011)

15. Richiardi, J., Bunke, H., Van De Ville, D., Achard, S.: Machine learning with brain graphs. *IEEE Signal processing magazine* 58 (2013)
16. Richiardi, J., Eryilmaz, H., Schwartz, S., Vuilleumier, P., Van De Ville, D.: Decoding brain states from fMRI connectivity graphs. *NeuroImage* 56(2), 616–626 (2011)
17. Salvador, R., Suckling, J., Schwarzbauer, C., Bullmore, E.: Undirected graphs of frequency-dependent functional connectivity in whole brain networks. *Philosophical transactions of the Royal Society of London. Series B, Biological sciences* 360(1457), 937–946 (2005)
18. Schwickert, H.C., Schweden, F., Schild, H.H., Piepenburg, R., Düber, C., Kauczor, H.U., Renner, C., Iversen, S., Thelen, M.: Pulmonary arteries and lung parenchyma in chronic pulmonary embolism: preoperative and postoperative CT findings. *Radiology* 191(2), 351–357 (1994)
19. Thieme, S.F., Becker, C.R., Hacker, M., Nikolaou, K., Reiser, M.F., Johnson, T.R.C.: Dual energy CT for the assessment of lung perfusion—correlation to scintigraphy. *European Journal of Radiology* 68(3), 369–374 (2008)
20. Thieme, S.F., Johnson, T.R.C., Lee, C., McWilliams, J., Becker, C.R., Reiser, M.F., Nikolaou, K.: Dual-Energy CT for the assessment of contrast material distribution in the pulmonary parenchyma. *American Journal of Roentgenology* 193(1), 144–149 (2009)
21. Thies, C., Metzler, V., Lehmann, T.M., Aach, T.: Formal extraction of biomedical objects by subgraph matching in attributed hierarchical region adjacency graphs. In: *Medical Imaging 2004. SPIEProc*, vol. 5370 (February 2004)
22. Tuder, R.M., Archer, S.L., Dorfmueller, P., Erzurum, S.C., Guignabert, C., Michelakis, E., Rabinovitch, M., Schermuly, R., Stenmark, K.R., Morrell, N.W.: Relevant issues in the pathology and pathobiology of pulmonary hypertension. *Journal of the American College of Cardiology* 62(25 SUPPL.) (2013)
23. Ukil, S., Reinhardt, J.M.: Anatomy-guided lung lobe segmentation in X-ray CT images. *IEEE Transactions on Medical Imaging* 28(2), 202–214 (Feb 2009)
24. Varoquaux, G., Gramfort, A., Poline, J., Thirion, B.: Brain covariance selection: better individual functional connectivity models using population prior. *Nips* 10, 2334–2342 (2010)
25. Zrimec, T., Busayarat, S., Wilson, P.: A 3D model of the human lung. In: *LNCS*, S. (ed.) *Proceedings of MICCAI 2004*. vol. 3217, pp. 1074–1075 (October 2004)